Two-Line Focused Laser Differential Interferometry of a Flat Plate Boundary Layer at Mach 6

Joshua M. Weisberger*, Brett F. Bathel†, Gregory C. Herring‡, Gregory M. Buck§, Stephen B. Jones¶, and Angelo A. Cavone‖
NASA Langley Research Center, Hampton, VA, 23606

Cylindrical optics have been added to a conventional two-point focused laser differential interferometry (FLDI) system to make measurements of density fluctuations at multiple points along two lines. Optics fixed in rotation mounts allow for the two lines to be oriented in any position relative to each other to make measurements of different physical phenomena. The system was first characterized in the laboratory using a laser-induced breakdown spark to provide a well-defined density fluctuation. The system was then installed at the NASA Langley 20 Inch Mach 6 Air Tunnel to make measurements through the boundary layer of a flat plate model and in the tunnel freestream.

I. Introduction

The focusing laser differential interferometer (FLDI) originally described by Smeets and George [1] is capable of providing time-resolved measurements of density fluctuations at a point. The instrument uses two closely-spaced, orthogonally-polarized, parallel beams that are transmitted from the pitch side of the instrument and focused to two small spots on the measurement plane. These points are separated by a distance Δx_{WP} as shown in Fig. 1. where blue and red represent separate, orthogonally-polarized laser light paths between the pitch and catch sides of the instrument. A small change in density, $\Delta\rho$, in the flow results in a proportional change in refractive index, Δn, as described by the Gladstone-Dale relation:

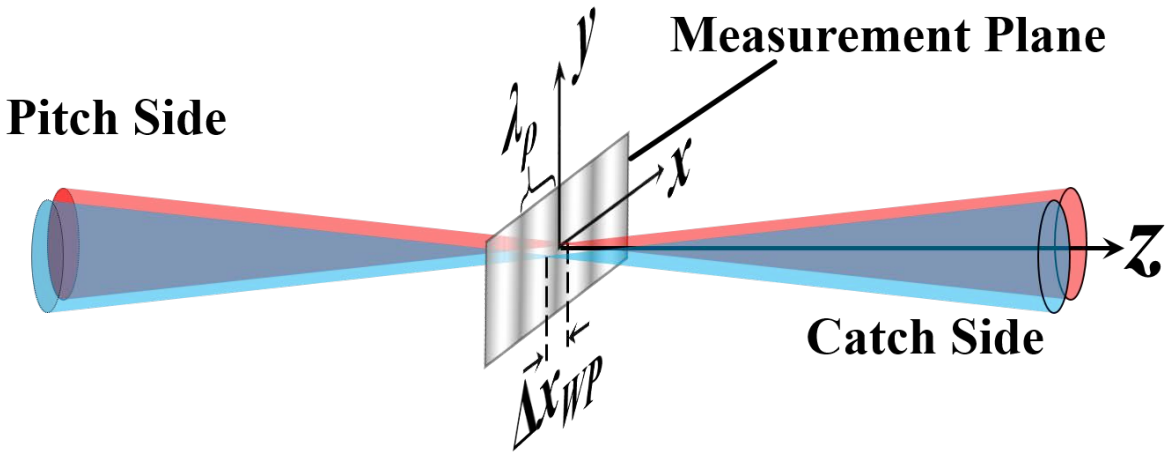

Fig. 1 Laser light paths for conventional FLDI between pitch and catch sides of the instrument.

*Research Engineer, Advanced Measurements and Data Systems Branch, AIAA Member.
†Research Engineer, Advanced Measurements and Data Systems Branch, AIAA Senior Member.
‡Research Physicist, Advanced Measurements and Data Systems Branch.
§Senior Researcher, Aerothermodynamics Branch, AIAA Associate Fellow.
¶Research Technician, Analytical Mechanics Associates.
‖Research Technician, Analytical Mechanics Associates.

$$\Delta n = K_{\text{air}} \Delta \rho \tag{1}$$

where $K_{\text{air}} = 2.3 \times 10^{-4}$ m^3/kg is the Gladstone-Dale constant for air. If a uniform difference in refractive index exists between the two focused spots persisting over some distance, s_z in the z-direction, then a phase difference is imparted between the two orthogonally-polarized beams according to:

$$\Delta \phi = \frac{2\pi}{\lambda_0} s_z \Delta n \tag{2}$$

where $\Delta\phi$ is the phase difference and λ_0 is the wavelength of the laser light. After the orthogonally-polarized laser light is combined on the catch side of the instrument, it is passed through a linear polarizing filter that is adjusted such that it transmits the polarization component corresponding to the middle of the interference fringe. The intensity of laser light incident on a high-speed photodetector will then change proportionally to $\Delta\rho$. Unlike path-averaged laser differential interferometers (LDI) that use collimated laser beams to sense density fluctuations [1–6], the FLDI has the benefit of attenuating the influence of density gradients away from the measurement plane on the measured signal. This attenuation of signal is the result of spatial filtering as the beam diameter of the laser light becomes large relative to density disturbance wavelength, λ_ρ [7–10]. Further discussions on the overall response of a single-point FLDI signal with the application of a series of transfer functions that are dependent upon disturbance wavenumber, $k_\rho = 2\pi/\lambda_\rho$, can be found in [7–12].

The single-point FLDI has been successfully applied to high-speed flow experiments in the last decade as advancements in high-speed analog-to-digital conversion instrumentation have enable acquisition rates in excess of tens of MHz. Such acquisition rates are critical to the understanding of high-speed flow, like hypersonic boundary layer transition-to-turbulence, where disturbances with frequencies in the 100s of kHz drive certain aspects of the flow physics. Azzazy at al. [13] were the first to demonstrate a variant of the single-point FLDI in an aerofoil boundary layer with a frequency response up to 1 MHz, analyzing the magnitude of the signal root-mean-square (RMS) to determine transition-to-turbulence location. Parziale et al. [11, 12, 14] performed the first modern single-point FLDI measurements in a hypersonic wind tunnel, providing analyses of the spectral behavior of both the tunnel freestream and wind tunnel model boundary layer disturbances up to 10 MHz. Numerous other examples of the application of the single-point FLDI can be found in [5, 7–9, 15–22].

One drawback of the single-point FLDI is its inability to measure density disturbance velocity, U_ρ. Data obtained with the instrument are first acquired as a time series and then a Fourier analysis is performed. The resulting spectra of the density disturbance field at a point in the measurement plane are given as a function of frequency, ν_ρ. However, in order to accurately determine the response of the instrument, the appropriate wavenumber-dependent transfer functions must be applied to the raw spectra. This requires that the frequency-dependent spectra to be recast as a function of wavenumber, $k_\rho = 2\pi\nu_\rho/U_\rho$, which requires U_ρ to be assumed or known. Smeets and George were the first to propose a two-point FLDI measurement where a polarizing Koester prism was used to generate two measurement points. More recent work using several different optics incorporated into a single-point FLDI instrument to generate two separate measurement points is described in Refs. [18, 23–26]. Two-point FLDI velocity measurements have also be obtained using two separate, single-point FLDI instruments as in Ref. [14].

For high-speed boundary layer measurements, multiple measurement points distributed throughout the boundary layer are preferable in order to provide a complete understanding of its state (e.g. laminar or turbulent) and characterize the distribution of disturbance intensities and velocities. Smeets and George [1, 2] and Smeets [3] were the first to propose a multi-point LDI that used a series of Wollaston polarization prisms to generate up to eight measurement points for the study of boundary layer flow. For the eight-point measurements in [3], an eight-channel photodiode array was used to record the time-varying signal from each point. Wadhams et al. [27] used a five-point FLDI system for measurements on a cone in a hypersonic flowfield, however it appear that these measurements were spaced sufficiently far apart such that correlated measurements could not be made. Recently, Hameed et al. [28] demonstrated a 4-point FLDI instrument used to characterize boundary layer flow over a cone in a Mach 6 flow. These points, generated using two additional Wollaston polarizing prisms, provided for measurement of the density disturbance spectra and phase velocity using two beam pairs located at two wall-normal positions within the boundary layer.

For measurements in the boundary layer above a broad, flat surface, the use of conventional laser beam focusing methods in an FLDI instrument may not be appropriate as portions of the beam can be truncated by the model itself. Recent work by Houpt et al. [16, 19] replaced the spherical optics of a conventional FLDI instrument with cylindrical focusing optics. This approach allowed for single-point density disturbance spectra to be obtained above a flat wall

boundary layer in a Mach 2 wind tunnel while maintaining a degree of spatial filtering for disturbances away from the measurement plane.

The purpose of this paper is to demonstrate the feasibility of a multi-point FLDI instrument for use in high-speed wind tunnel experiments where tunnel or model geometry would otherwise interfere with the spherically-focused beams of a conventional FLDI instrument. In this work, we use a combination of spherical and cylindrical focusing optics to form a pair of closely-spaced, orthogonally polarized lines (as opposed to two spots) on the measurement plane as shown in Fig. 2. Careful selection of the focal lengths of the cylindrical optics allows for the control of the line pair height, Δy_L, on the measurement plane. Signals from density disturbances at 16 points across the length of this line pair are acquired using a 16-element linear photodiode array. The addition of a Nomarski polarizing prism, as used in Refs. [18, 26], enables measurements from density disturbances along two closely-spaced line pairs, separated by Δx_{NP} in the x-direction. A cross-correlation, or similar analysis, of the time-varying signals at the same relative locations along both line pairs provides for a measurement of the phase velocities, $U_\rho\,(y,t)$. Two experiments are performed to demonstrate the performance of this instrument. In the first experiment, measurements with the single- and two-line-pair configuration oriented both parallel and normal to the surface of a traveling shockwave formed from a laser spark are obtained. The time varying signals and velocities obtained with the multi-point FLDI instrument are then compared to results obtained simultaneously with a high-speed schlieren system framing at 400 kHz. In the second experiment, single- and two-line measurements in the boundary layer of a flat plate in a Mach 6 flow are obtained in the wall-normal direction. High-speed schlieren images and time-averaged Pitot pressure rake data from the flat plate flow are used to verify the boundary layer thickness estimate obtained with the multi-point FLDI instrument.

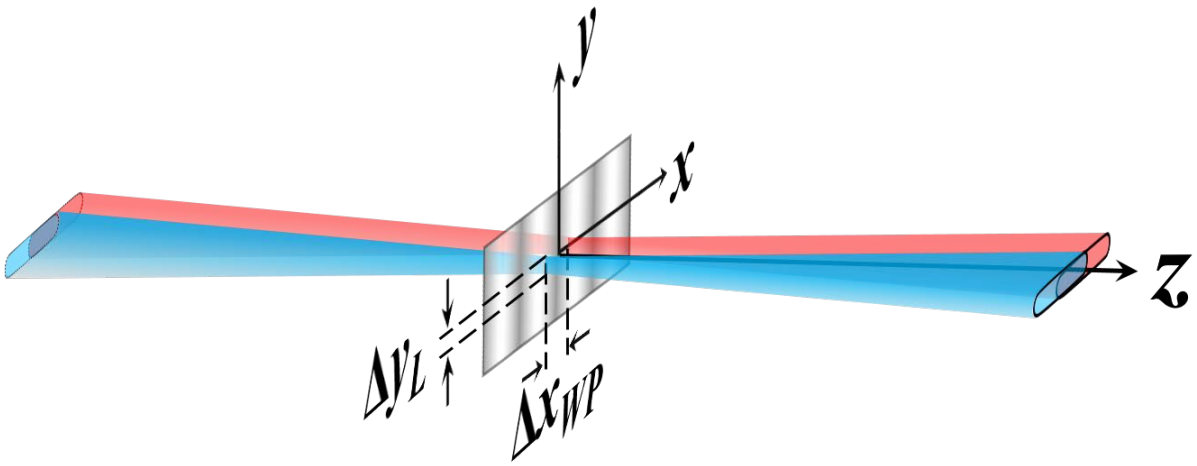

Fig. 2 Laser light paths for multi-point FLDI instrument between pitch and catch sides of the instrument.

II. Experimental Setup

A. Line-FLDI System

A schematic of the two-line, multi-point FLDI (2L-FLDI) system is shown in Fig. 3, with the transmitter/pitch side, P, to the left of measurement plane (section A-A) and the receiver/catch side, C, to the right. A single-mode, vertically polarized $\lambda_0 = 532$ nm laser, L, with maximum output power of 300 mW reflects off two turning mirrors, $\mathrm{M}^{1\mathrm{P}}$ and $\mathrm{M}^{2\mathrm{P}}$, onto the optical axis of the system. A half-wave plate, $\mathrm{HWP}^{1\mathrm{P}}$, polarizing beamsplitter cube, PBS, and beam dump, BD, are used to adjust the laser power that is transmitted into the system. A second half-wave plate, $\mathrm{HWP}^{2\mathrm{P}}$, rotates the polarization angle by 45° relative to the y-axis. A short focal length spherical lens, BE, is then used to expand the beam in all directions. Next, a Nomarski prism, NP, splits the vertical and horizontal components of polarization by a small angle about the z-axis in the xz plane and then redirects them such that they cross the z-axis in the xz plane ≈ 267 mm

beyond the prism's exit plane. These orthogonally-polarized beams are denoted in the schematic with either blue or red. After NP, a third half-wave plate, HWP^{3P}, rotates the polarization angle of each beam such that they are oriented at ±45° relative to the y-axis. Up to this point, the instrument is essentially identical to the two-point FLDI system described in Bathel *et al.* [30].

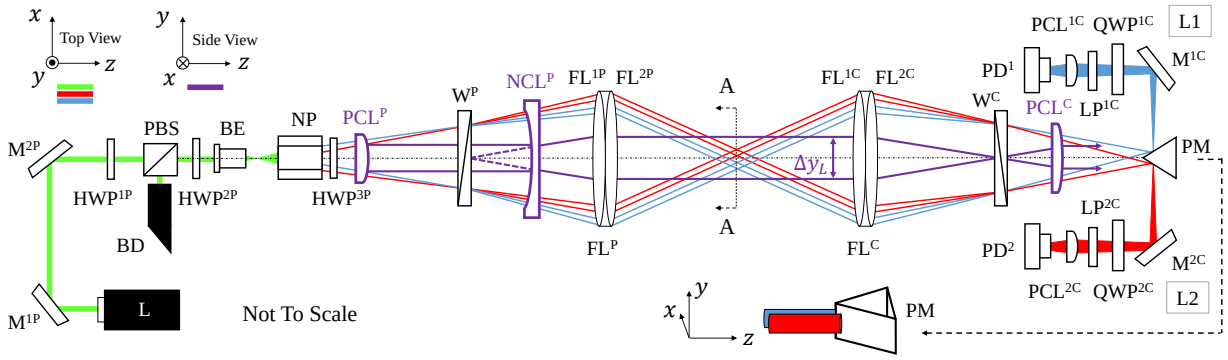

Fig. 3 Schematic of the two-line FLDI system, with the transmitter side on the left and the receiver side on the right.

However, after HWP^{3P}, a series of cylindrical lenses are placed at various positions along the instrument's optical axis so that lines of focused laser light are formed parallel to the y-axis on the measurement plane. The first of these is a positive cylindrical lens, PCL^P , that is placed so that it collimates the beams with respect to the y-axis while allowing them to continue to expand in the $\pm x$-directions. In Fig. 2, the magenta color is used hereafter to describe the propagation of the laser beams when viewed orthogonally to the yz plane. For reference, the coordinate system orientations for all colors used in the schematic is shown in the top left of Fig. 2. A Wollaston prism, W^P, placed at the crossing point of the two beams formed by NP further splits each beam by 2 arc minutes relative to the z-axis and parallel to the xz plane. This creates two additional orthogonally-polarized beams. A negative cylindrical lens, NCL^P, is then placed one focal length from W^P to further expand the beam in the $\pm y$-directions. A field lens, FL^P, consisting of two back-to-back achromatic doublets, FL^{1P} and FL^{2P}, is used to focus the beams in the xz plane and collimate them in the yz plane. This is placed at one effective focal length (EFL) from W^P such that the central axis of each beam propagates parallel to one another and the z-axis after exiting FL^P. Using this configuration, two line pairs (each referred to as a Wollaston pair) are formed on the measurement plane (section A-A), with each line oriented parallel to the y-axis and separated in the x-direction by $\Delta x_{WP} = 172.6\ \mu$m. The two Wollaston pairs (referred to as a Nomarski pair) are separated by $\Delta x_{NP} = 1.842$ mm. Here it is important to note that the length of the lines, Δy_L, can be specified with careful selection of BE, PCL^P, and NCL^P focal lengths.

Beyond the measurement plane (section A-A) in Fig. 3, light from laser lines diverges in the $\pm x$-directions and remains collimated in y. A second field lens, FL^C , consisting of back-to-back achromatic doublets, FL^{1C} and FL^{2C}, is then placed at a distance from the measurement plane equal to that between FL^P and the measurement plane. For this work, both FL^P and FL^C are identical. After passing through FL^C , the beams are focused in both the x- and y-directions. Another 2 arc-minute Wollaston prism, W^C, is placed at the EFL of FL^C to combine the orthogonally-polarized beams from each Wollaston pair. The location of W^C also corresponds to the focus of the laser light in the y-direction. After passing through W^C, the laser light begins to diverge in the y-direction. This light is then collimated in y by placing a positive cylindrical lens, PCL^C, one focal length from W^C. Beyond PCL^C the laser light from the Nomarski pair continues to converge in the x-direction until two focused laser lines are formed. The light from these lines, offset from one another by a small distance in x, are then split into two separate legs of the instrument, L1 and L2, with a right-angle prism mirror, PM. An isometric view of this splitting of the two laser lines with PM can be seen at the bottom right of the schematic. After PM, both legs L1 and L2 contained the same optical components. First a turning mirror, $M^{\#C}$, redirects the beam by 90° and can be adjusted for alignment on to the detector. The beam then passes through a quarter-wave plate, $QWP^{\#C}$, that is adjusted to remove any ellipticity in the polarization of the beam. Next a linear polarizer, $LP^{\#C}$, makes the two overlapping orthogonally-polarized beams interfere with one another, and a short focal length positive cylindrical lens, $PCL^{\#C}$, is used to adjust the thickness of the laser line incident on the linear silicon PIN photodiode array, $PD^{\#}$. Here it is important to note that careful selection of the focal length of PCL^C determines the length of the laser line incident on $PD^{\#}$. For the experiments described in this work a 16-element silicon PIN photodiode

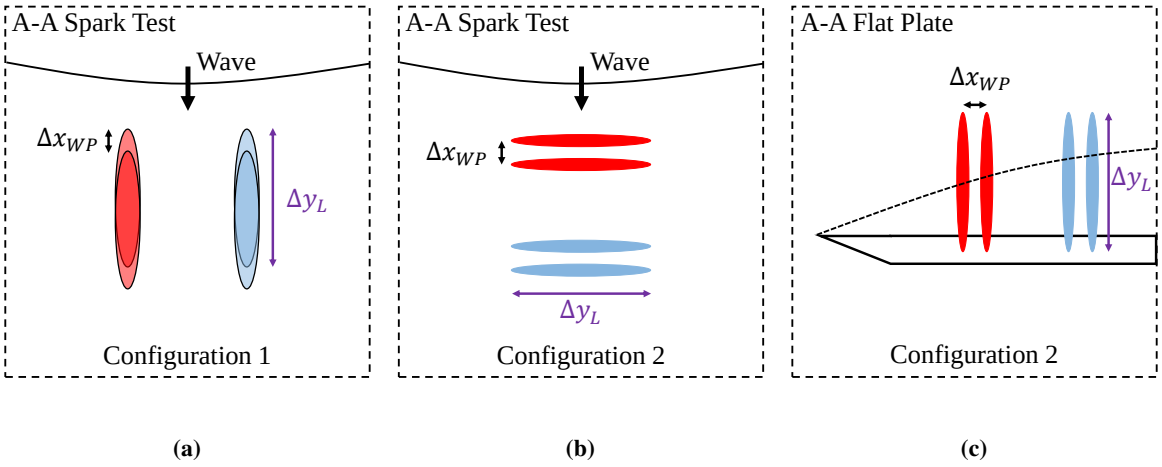

Fig. 4 Laser line orientations obtained with the two-line, multi-point FLDI instrument. The spark test configurations are shown in (a) and (b), while the flat plate test is shown in (c).

array was used, with each element measuring 0.8 mm high (active area 0.7 mm) for a total height of 12.8 mm and a total width of 2.0 mm. Therefore, the focal length of PCL^{C} was selected in order to slightly overfill $\text{PD}^{\#}$ in the $\pm y$-direction.

The orientation of the two laser lines can be changed to address the particular measurement needs for a flow. Figure 4 shows two laser line orientations applied to three configurations that were achieved with the instrument and are later described in Sections III and IV. Figure 4a shows a configuration (Configuration 1) that can be used if sequential measurements of an evolving density wave are desired. Here, WP and WC are rotated such that the laser lines within each Wollaston pair overlap one another, with an overlap offset of Δx_{WP}. The NP is then rotated such that the overlapping laser lines in each Wollaston pair are separated by Δx_{NP} relative to the their minor axes. Figures 4b and 4c show a configuration (Configuration 2) that can be used if measurements are desired across a spatially-varying disturbance field, relative to the laser line pair's (Wollaston pair's) major axes, with the dominant phase velocity component oriented parallel to the Wollaston pair's minor axes. Here, W^{P} and W^{C} are rotated such that the laser lines within each Wollaston pair are separated by Δx_{WP} relative to their minor axes. The NP is then rotated so that the Wollaston pairs are separated by Δx_{WP} relative to the minor axes of the laser lines. For the experiments performed in this work, the 90° rotation of the Nomarski pair shown between Figs. 4b and 4c was accomplished by rotating the following optics by 90° about the instrument's optical axis: HWP^{2P}, NP, HWP^{3P}, PCL^{P}, W^{P}, NCL^{P}, W^{C}, and PCL^{C}. Additionally, the PM and all subsequent optics in legs L1 and L2 were mounted together and connected with a rotation mount to the catch side of the instrument such that they could all be rotated by 90° about the instrument's optical axis.

B. Knife-Edge Calibration

In order to compute the velocity of a disturbance as it passes through two adjacent measurement locations, the distance between those locations is needed with high accuracy. In a two-point FLDI system, determination of the separation distance between the two points is simple; the method used by Bathel *et al.* [26] uses a CMOS camera located at the focus (measurement plane) of the system to image the focused spots with a resolution of 3.45 μm per pixel. Measuring the distance between adjacent measurement points in the laser line is more difficult since there are no edges in the laser line to delineate separate channels; it is one continuous laser line with varying intensity. The separation of the line into contiguous channels is performed by the photodiode linear array itself. The spacing of the photodiode elements themselves is not a measure of the actual separation of the channels in physical space, since the beam can be magnified (larger or smaller) when focused onto the photodiode element. A linearly-traversing knife-edge system was used to obtain the channel spacing in physical space.

The channel spacing measurement system comprises a razor blade (knife-edge, KE) fixed to a linear stage actuator. The initial position of the KE is completely out of the beam path, so that all light passes through to the detector. The actuator is then traversed in steps of 100 μm along the length of the laser line's major axis until the beam is entirely blocked from passing through to the detector. When the KE is not blocking the channel, the signal measured by the

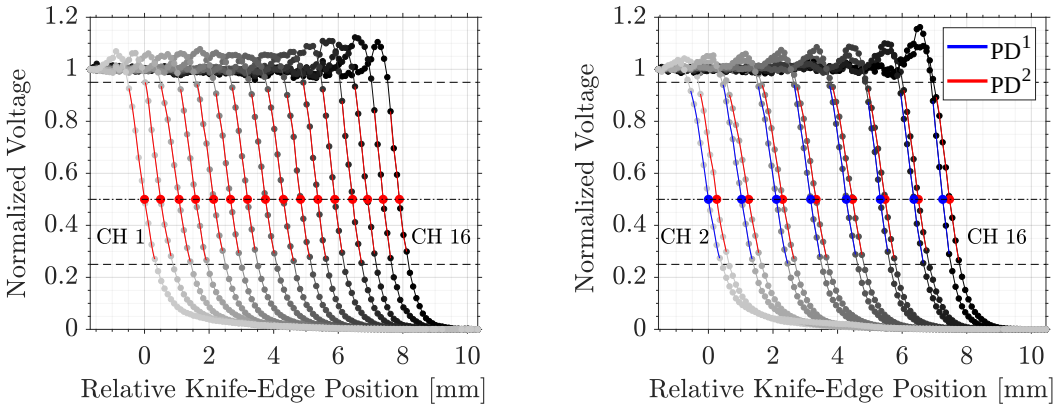

(a) (b)

Fig. 5 Knife-edge calibration results for (a) data set 14 and (b) data set 15.

detector is at its maximum. As the KE moves through the channel, the signal measured by the detector decreases continuously until the channel is completely blocked, at which point the detector measures its minimum signal.

The results of two KE calibration measurements are shown in Fig. 5. In Fig. 5a, a single photodiode with all 16 channels is used, whereas in Fig. 5b, two photodiodes are used, each with only the even channels connected to the scope (since the maximum number of channels that could be acquired at a time was 16). In both plots, increasing channel number is denoted with darkening lines. The circles denote the actual positions where the knife-edge was moved to and data acquired. The y-axis in each plot is normalized voltage (between 0 and 1), which is obtained by normalizing each channel by its own maximum and minimum voltage signal when the knife-edge is completely removed from (or inserted into) the system, as shown in Eq. (3).

$$V_{\text{norm}} = \frac{V_{\text{cal}} - V_{\text{min}}}{V_{\text{max}} - V_{\text{min}}} \tag{3}$$

The data for each channel between a normalized voltage of 0.25 and 0.95 is fit with a low-order polynomial (red or blue line). The difference in position between adjacent channels at $V_{\text{norm}} = 0.5$ (red or blue circles) gives the physical channel separation in space, and is equivalent to the Nomarski pair beam separation from [18, 26]. The mean channel spacing from the data in Fig. 5a is 526 ± 66 μm. The mean channel spacing from the data in Fig. 5b is 1.036 ± 0.145 mm for PD^1 and 1.030 ± 0.111 mm for PD^2, noting that this spacing will be approximately double that of Fig. 5a because only the even channels are being sampled. These channel spacing values are used in calculations of the velocity of the disturbances.

C. Laser Induced Breakdown Spark Test

The ability of the system to determine the shape and speed of a weak disturbance is determined using a shock wave generated by laser-induced breakdown (LIB). The FLDI system is used in conjunction with a high-speed schlieren (HSS) system and a high-power 532 nm laser (EverGreen) to generate the spark. Two orientations of the two-line FLDI system are tested, as shown in Fig. 4a and Fig. 4b.

A BNC Model 577 (4-channel) digital delay/pulse generator was used for triggering the LED, SA-Z, EverGreen, and the FLDI system. The main system clock pulse output was set to 400 kHz. One channel controls when the camera triggers, and is synced to the system clock so it always runs at 400 kHz. Another channel controls the LED triggering indirectly through the camera software. A third channel triggers the EverGreen laser and the FLDI scope. The full frame size of the camera sensor is 1024×1024, but in order to run at 400 kHz, the FoV was cropped to 256×80. The oscilloscope was used to acquire a data set at every trigger, ensuring accurate correlation between the schlieren sequence and the FLDI time record. Insulated 6 ft 50 Ω BNC cables (L-Com, CCTN5806B) terminated at 50 Ω were connected to the photodiodes, and the sampling rate was 50 MHz with a record length of 50 MS.

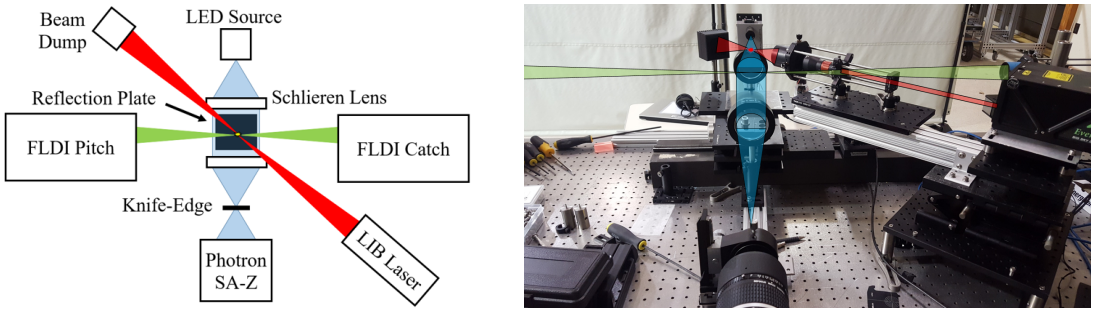

(a) **(b)**

Fig. 6 Spark test (a) schematic top-view and (b) picture from behind schlieren camera (SA-Z), with light beams shown in green (FLDI), blue (HSS) and red (LIB).

D. 20 Inch Mach 6 Setup

The FLDI system was installed at the 20 Inch Mach 6 Air Tunnel to take data during testing of a flat plate model. Large 80/20 T-slotted aluminum cages were used to mount the FLDI breadboards, and were isolated from the tunnel to reduce vibrations. An accelerometer was mounted to the catch board to monitor the vibrations. The pitch board (Fig. 7a) and the catch board (Fig. 7b) were both placed on two z-axis translation stages to enable precise vertical alignment of the laser beams with respect to the flat plate model used in the tests. The use of two stages for each board also allowed for precise leveling of the boards to ensure the laser traversed the flat plate parallel to its surface. On the catch board, the two enclosures housing the linear array photodiodes can be seen. For each run, 16 channels of data were acquired using a National Instruments (NI) PXIe-1062Q chassis with two 8-channel scope modules (Fig. 7c). Each channel that was recorded by the scope passed through a 4.5 MHz low-pass filter (red tubes in Fig. 7c).

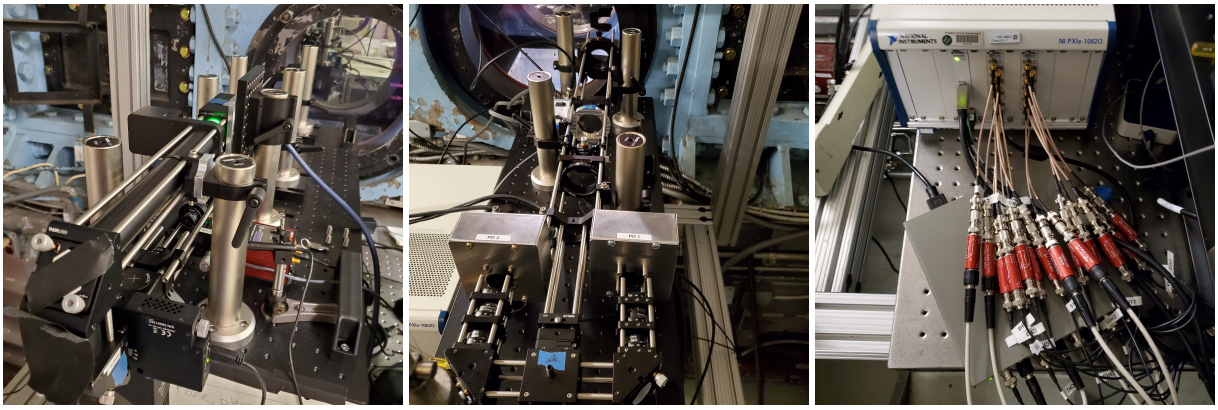

(a) **(b)** **(c)**

Fig. 7 FLDI setup at the 20 Inch Mach 6 Air Tunnel, including images of (a) the pitch board, (b) the catch board, and (c) the NI scope with all 16 channels attached, with 4.5 MHz filters for each.

E. Photodiode Channel Cross-Talk

Measurements were conducted to ensure that each channel was not subjected to cross-talk from an adjacent channel. Four channels near the center of the photodiode were used (channels 7, 8, 9, and 10), and a knife-edge selectively blocked each channel one-by-one, directly in front of the photodiode itself (in contrast to the element spacing calibration from Section II.B). A small compressed air turbulent jet was used to provide the density fluctuations at the laser beam

focus. The power spectral density of all the channels was plotted to evaluate their influence on each other. Figure 8 shows four separate plots, one for each channel. For each plot, five data sets are shown, ranging from the knife-edge not blocking any channels (black) to the knife-edge blocking all of the channels (magenta). Because the knife-edge was introduced from the top of the photodiode (lower channel numbers), it was not possible to block, for example, only channel 8 without also blocking channel 7.

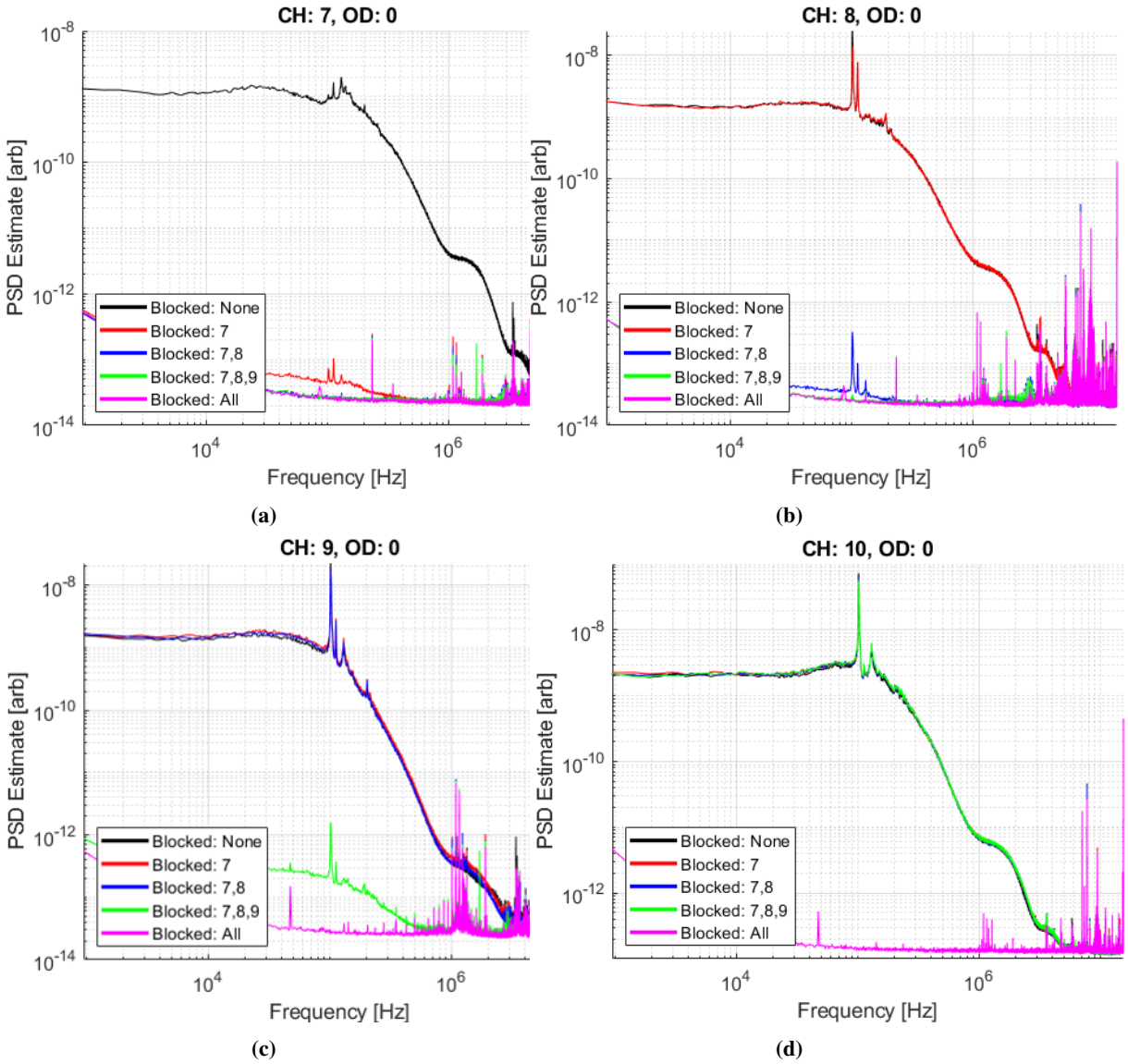

Fig. 8 Photodiode cross-talk power spectral density plots for channel (a) 7, (b) 8, (c) 9, and (d) 10.

The magenta line in each sub-figure of Fig. 8 represents the noise floor of the photodiode, since in this condition no laser light is incident on the photodiode, as it is being blocked completely by the knife-edge. In Fig. 8a, the only data set with signal is when the knife-edge is not blocking any channels. In Fig. 8b, non-zero signals can be seen for both the knife-edge-out case and when the knife-edge is blocking channel 7. The signal for those two cases are nearly identical, indicating that channel 7 does not have any influence on the signal registered on channel 8. Similar results can be seen in Fig. 8c and Fig. 8d, where the signals remained unchanged as adjacent channels were covered by the knife-edge. These results indicate that there is negligible cross-talk between the individual elements (channels) on the photodiodes, and their results can be interpreted independently.

F. Beam Location on Flat Plate

The determination of the boundary layer thickness depends on the distance of the measurement location downstream from the leading edge of the plate. To compare the boundary layer profile with measurements from the FLDI system, the location of the photodiode channels in relation to the surface of the flat plate must also be accurately determined. To measure the location of the channels relative to the surface of the flat plate, a similar knife-edge system as the channel spacing calibration was used, with a linear traversing actuator to which a knife-edge was attached. The measurement had to be made with the FLDI system in place and the model injected. The actuator/KE system was fixed to the model surface, which was then injected into the tunnel and the laser allowed to pass over the model surface. The actuator was controlled remotely and was traversed in steps of 250 μm perpendicular to the surface along the major axis of the laser line, taking measurements on all channels at every step. For every data set, the mean voltage was obtained from the 1-second acquisition raw data and plotted versus the knife-edge position in Fig. 9a. The channel legend can be seen in Fig. 9b, which shows the approximate position of the linear array photodiode relative to the flat plate model surface. From the data, it appears that channels 14 through 16 are covered by the edge of the model, while channels 13 through 1 pass over the top of the model surface to the other side.

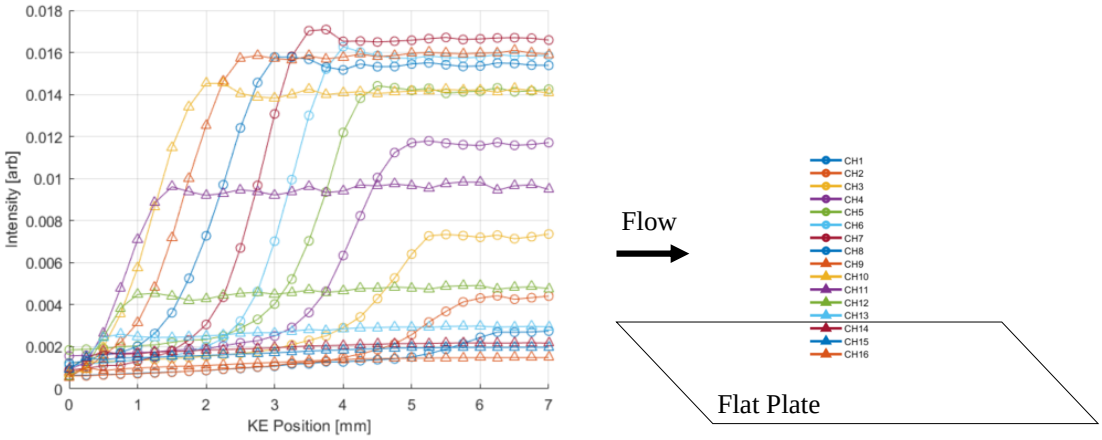

(a) **(b)**

Fig. 9 Determination of the beam location relative to the flat plate model, with (a) showing the voltage measured on each channel during knife-edge retraction, and (b) showing the approximate location of the beam with respect to the model edge/surface.

III. Spark Test Results

A. Configuration 1

A single spark experiment consisted of a single instance of the LIB-generated wave, with data acquisition for both the FLDI system and the HSS system. For configuration 1, 50 instances of the spark experiment were run. As the wave expanded from the LIB spark location, it was first registered on channel 1, and was last registered on channel 16, passing through the other intermediate channels along the way. A plot of a single spark experiment data can be seen in Fig. 10a. These data sets have been shifted to zero on the y-axis by subtracting each channel's mean voltage from before the wave arrival. This is done solely for visualization purposes, since the mean voltage for each channel follows the typical Gaussian distribution of the beam intensity along the line. This Gaussian beam intensity can still be seen in the maximum voltage for each channel, with the outer channels (1 and 16) reading less signal than the inner channels. Due to the linear array orientation, the first channel to register a change in the voltage is channel 1. In the raw voltage data, there appears to be a repetitive low amplitude disturbance, which comes from the pulsing of the high-power LED used for the simultaneous HSS. While these disturbances do not affect the FLDI results, data was also taken without the HSS running, and this coupled disturbance in the FLDI data disappears.

The distance in physical space at the measurement location was obtained using the knife-edge calibration method described in Sec. II.B. To compute the velocity of the wave traversing the channels of the linear array, the time shift between the data sets is needed. The peak times of the raw voltage data from Fig. 10a are used. A second-order polynomial is fit to the data in the region near the peak, and the time at which the peak occurs is determined for each channel. A plot of the channel distance versus the channel peak time is shown in Fig. 10b with black squares (left axis). The velocity from one channel to the next is simply the slope of the line connecting the two points. A fit of all the data points (dashed black line) gives the mean wave velocity as it passes along the laser line. Using all 50 data sets for each channel, the mean and standard deviation of all the velocities from the fit is 346.05 ± 0.26 m/s. This can be compared to the sound speed in air at the temperature in the laboratory when the data was taken (76°F) of 345.8 m/s.

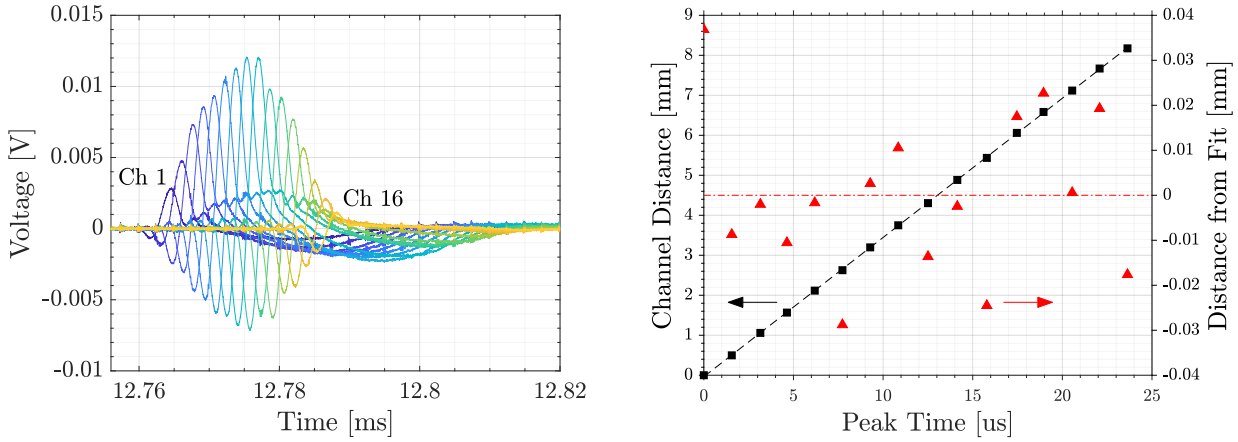

(a) **(b)**

Fig. 10 Configuration 1 (a) raw voltage that has been zeroed by its mean, and (b) channel position versus the peak time to fit the velocity slope.

Small changes in the peak time or the channel separation distance result in relatively large changes in the velocity. The right axis of Fig. 10b shows the offset of each channel distance from the linear fit. While these offsets are small (on the order of tens of microns), the corresponding velocity offset from the mean is quite large (on the order of tens of meters per second). This can more clearly be seen by simply taking the forward difference between adjacent channels to compute the slope, and thus velocity of the wave as it passes through the laser line. In Fig. 11, the computed velocity from this forward difference is shown with red squares, and the sound speed in the laboratory as the dashed black line. A table with the mean velocities for each channel-pair is shown in Table 1. From both figure and table, it can be seen that the mean velocities for each channel pair deviate substantially from the sound speed, but the precision for each channel pair over 50 separate spark experiments is very good. Since the channel-pair spacing is constant from the knife-edge calibration, this indicates that the relative peak times are extremely consistent over all experiments.

B. Configuration 2

The orientation of the beams for the second configuration of the spark experiment is shown in Fig. 4b. For these tests, only the even channels of both photodiodes were used (2, 4, 6, 8, 10, 12, 14, 16). In this orientation it was possible to take an image of the line pairs using a CMOS camera at the beam focus. From this image, the Wollaston beam-pair separation distances are $\Delta x_{\mathrm{WP}} = 172.6$ μm for the top beam and $\Delta x_{\mathrm{WP}} = 172.8$ μm for the bottom beam. The Nomarski beam-pair separation distance is $\Delta x_{\mathrm{NP}} = 1.842$ mm.

The raw voltage data on the even channels of both PD^1 and PD^2 can be seen in Fig. 12a. The top photodiode responds to the wave first, and is shown in red corresponding to the schematic in Fig. 4b. The bottom photodiode responds to the wave a short time after, and is shown in blue. Both signals have the characteristic immediate spike as the shock wave arrives, with an expansion tail, and then the return back to ambient conditions. This is the same structure that was observed in the two-point FLDI system in Bathel *et al.* [26]. This is also the structure seen in CFD simulations.

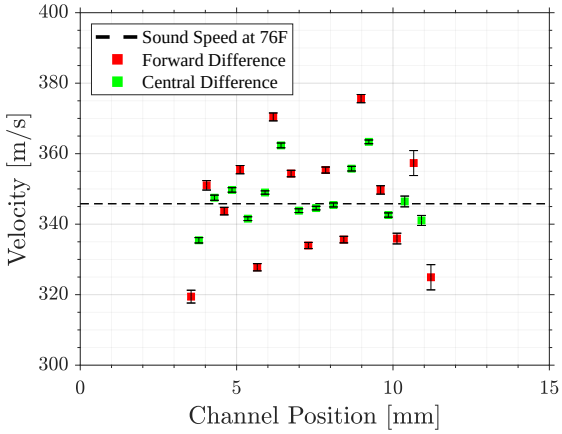

Fig. 11 Velocity from FLDI for LIB spark experiment for both forward and central difference calculations.

Table 1 Velocity comparisons from FLDI and HSS for configuration 1 (HSS results will be added).

Channel	V_{FLDI} [m/s]	V_{HSS} [m/s]	Channel	V_{FLDI} [m/s]	V_{HSS} [m/s]
1 – 2	319.45 ± 1.82	-	9 – 10	355.36 ± 0.85	-
2 – 3	351.02 ± 1.35	-	10 – 11	335.62 ± 0.93	-
3 – 4	343.71 ± 1.07	-	11 – 12	375.62 ± 1.17	-
4 – 5	355.47 ± 1.17	-	12 – 13	349.72 ± 1.20	-
5 – 6	327.78 ± 1.03	-	13 – 14	335.92 ± 1.52	-
6 – 7	370.43 ± 1.13	-	14 – 15	357.34 ± 3.54	-
7 – 8	354.36 ± 0.92	-	15 – 16	324.94 ± 3.58	-
8 – 9	333.95 ± 0.87	-			

The data in Fig. 12a has been shifted to zero on the y-axis using the mean voltage of the channel's signal before the wave arrives, as was done in Section III.A. The amplitude differences between each channel of a photodiode are still visible, and follow the familiar Gaussian distribution of the line of laser light. A zoom-view of the initial spike for both photodiodes is shown in Fig. 12b. The data is now colored differently, where a single color indicates the same channel on PD^1 and PD^2. For instance, the dark blue curve represents channel 2 on both PD^1 and PD^2. The curvature of the spherical shock wave can be seen in this data set, where the central channels register signal first, and the outer channels register signal a short time later. This data set also shows that the FLDI line was centered directly below the spark, since corresponding channels on opposite sides of the detector have very nearly the same delay (i.e. channels 2/16, 4/14, etc.).

To determine the velocity of the wave from the FLDI data, the spacing between the two photodiodes parallel to the wave path is needed, along with the time between the corresponding channel's peaks. For each channel, the data near the maximum voltage is fit with a low-order polynomial, and the peak time obtained from the maximum value of the fit. The change in time, dt, is computed by taking the difference between the corresponding channel's peak times from each photodiode, $dt = t_{\mathrm{ch,PD1}} - t_{\mathrm{ch,PD2}}$. The separation distance between the two photodiodes is the Nomarski pair separation distance, Δx_{NP}.

The resulting velocity from each channel pair between the top and bottom FLDI line is shown in Table 2 in the central column. Although there is only a single set of schlieren images for every FLDI data set acquired, the schlieren velocities shown in the right column of Table 2 correspond to the channel location in the schlieren FOV, and schlieren signal is averaged over the width of the corresponding channel. The velocity of each FLDI channel is quite consistent, with high precision over the 50 individual spark tests as indicated by the uncertainty of each channel. The HSS velocities are close to the FLDI velocities, but trend a little higher in general, by approximately 2 m/s.

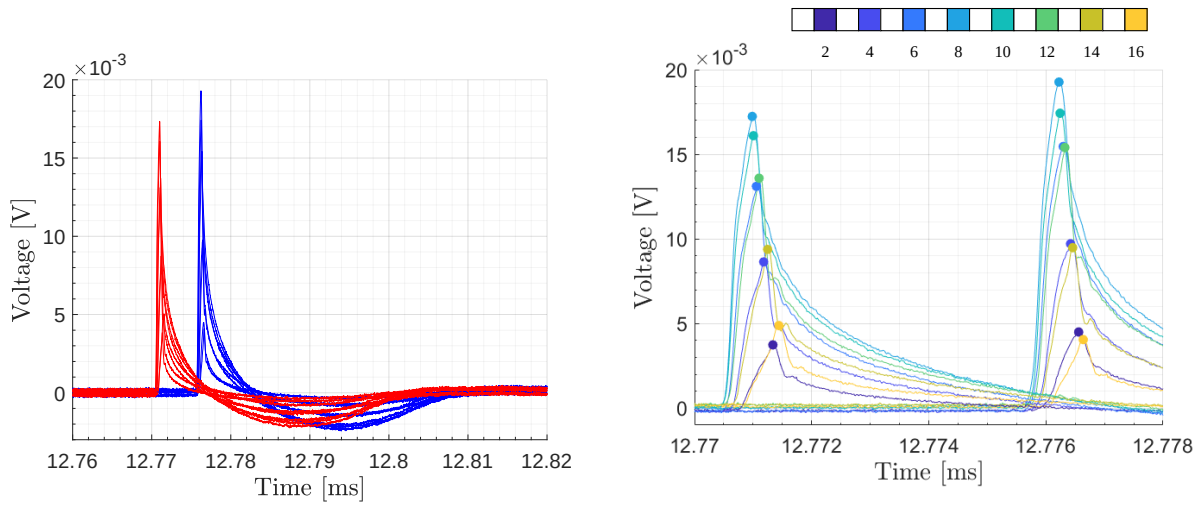

(a) **(b)**

Fig. 12 Configuration 2 (a) raw voltage for both photodiodes and (b) zoom-view of the channels colored by corresponding channels on both photodiodes, and with their peak times identified.

Table 2 Velocity comparisons from FLDI and HSS.

Channel	V_{FLDI} [m/s]	V_{HSS} [m/s]	Channel	V_{FLDI} [m/s]	V_{HSS} [m/s]
2	352.75 ± 0.23	356.94 ± 11.64	10	351.57 ± 0.15	352.97 ± 9.62
4	351.35 ± 0.16	353.37 ± 6.63	12	352.60 ± 0.09	355.62 ± 5.59
6	351.45 ± 0.33	354.16 ± 11.46	14	353.32 ± 0.23	352.97 ± 3.93
8	351.46 ± 0.13	353.31 ± 3.34	16	354.34 ± 0.15	355.73 ± 5.52

IV. 20 Inch Mach 6 Results

A. Run Summary

The FLDI testing was completed as a subset of a larger testing campaign which included other measurement techniques. FLDI data was obtained for runs 41 to 69, and high-speed schlieren data was obtained for some of the important FLDI run conditions in runs 70 to 75. A summary of the Reynolds number conditions for each run, as well as other run characteristics, can be seen in Table 3. The flat plate model was modular, with removable side rails (one on each side of the model), removable trip inserts near the leading edge, and a removable rake behind the FLDI measurement location. Detailed drawings of the model will be provided in the final paper.

Table 3 Reynolds number and other characteristics for all runs at 20 Inch Mach 6.

Re ($\times 10^6$ ft^{-1})	Runs	Characteristic	Runs
Re = 2.0	42,43,45,48,50-53,57,58,61,63,65,67,71,73,75	Side Rails On	41-64,72-75
Re = 3.0	56	Side Rails Off	65-71
Re = 4.0	49,54,59,62,64,66,68-70,72,74	Trips On	57-62,67-69,72,73
Re = 5.6	55	Trips Off	41-56,63-66,70,71,74,75
Re = 7.2	41,44,46,47	Rake Installed	41-56
		Rake Not Installed	57-75

B. Freestream Repeatability

Freestream measurements were taken for each run of data, after the model was retracted. The noise (and PSD) of the freestream is an important factor when trying to understand transition mechanisms. For repeatable runs at the same conditions, the freestream spectrum should remain unchanged. An example plot of the PSD estimate for Run 64 is shown in Fig. 13. While the absolute amplitudes of the PSD are different for each channel (due to the difference in signal intensity across the photodiode), the general trend of the freestream noise is the same, showing a flat response at lower frequencies, and a steady roll-off at higher frequencies. Further comparisons will be made with data sets from every run in the final paper.

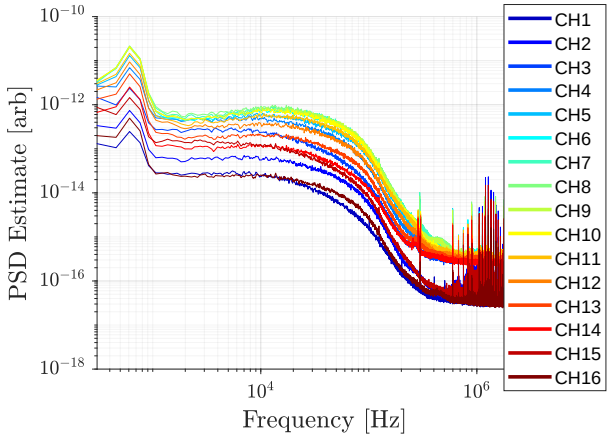

Fig. 13 Run 64 freestream PSD for all 16 channels.

C. Boundary Layer Measurements

To determine which channels were being blocked by the flat plate model, data was taken with the model first retracted and then injected, as shown in Fig. 14a where the mean voltage is plotted for each channel from a one second time series of acquired data. The lower number channels are farther above the surface of the model. The signal from channels 1 to 9 does not change appreciably between the two scenarios, but as the channel number increases, the signal on the higher channels drops when the model is injected. However, note that the signal does not drop to near-zero which would generally be associated with a hard edge. From the data in Section II.F and Fig. 9, it can be assumed that the surface of the model lies somewhere between channels 13 and 14. More analysis will be performed for the final version of the paper.

Measurements were taken during the run with the model injected to obtain the boundary layer profile. Data shown in this section is for Run 64, which had a Reynolds number of 4.02×10^6 ft^{-1}. The RMS voltage is computed for each channel after normalizing the data based on the Gaussian intensity distribution of the signal on the linear array photodiode. Figure 14b shows a plot of the channel number versus the RMS voltage. The dark gray box indicates the probable location of the model edge, and the light gray box indicates that the exact surface location between channels 13 and 14 cannot be determined. The RMS voltage is high near the surface, and decreases away from the surface. The freestream RMS voltages for each channel are also plotted, and show a nearly steady value for every channel. It is expected that outside the boundary layer, the RMS voltage would equal that of the measured freestream, and this is what is shown for channels 8 to 1. Many more data sets will be analyzed in the final paper, for both laminar and turbulent cases, over a range of different Reynolds numbers, with/without trips, and with/without side rails. Comparisons will also be made to high-speed schlieren measurements and to rake data.

Acknowledgments

This work was supported by the NASA Hypersonic Technology Project (HTP) and the Transformational Tools and Technologies (TTT) project. The authors would like to thank Mark Kulick for his assistance in the fabrication of

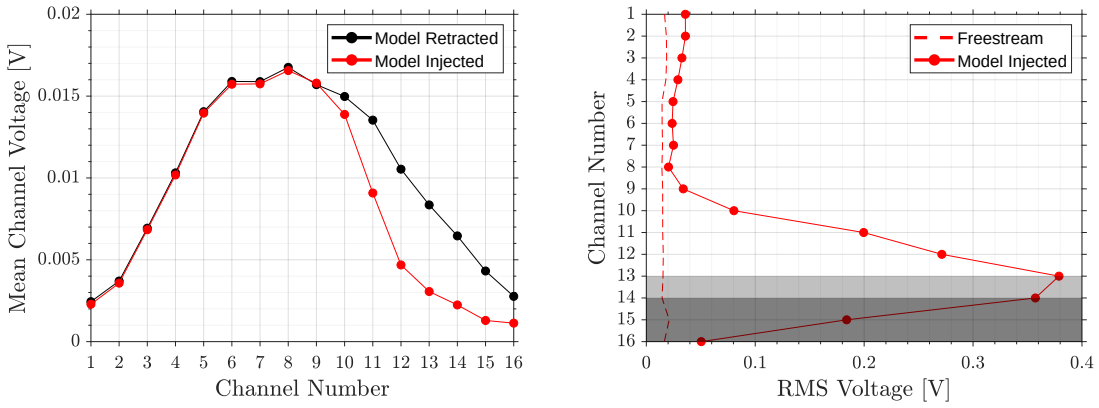

(a) **(b)**

Fig. 14 Figures of (a) mean voltage for each channel and (b) boundary layer profile based on RMS voltage.

numerous hardware components that were used in this work. Support for this test was provided by facility technicians and engineers: Johnny Ellis, Kevin Hollingsworth, Larson Stacy, and Sheila Wright, and Jonathan Crider.

References

[1] Smeets, G., "Laser-Interferometer Zur Messung An Achnellveranderlichen Schwachen Phasenobjekten," *Optics Communications*, 1970.

[2] Smeets, G., "Laser Interferometer for High Sensitivity Measurements on Transient Phase Objects," *IEEE Transactions on Aerospace and Electronic Systems*, Vol. AES-8, No. 2, 1972, pp. 186–190.

[3] Smeets, G., "Flow Diagnostics by Laser Interferometry," *IEEE Transactions on Aerospace and Electronic Systems*, 1977. doi:10.1109/TAES.1977.308441, URL `https://ieeexplore.ieee.org/document/4101772`.

[4] Salyer, T. R., Collicott, S. H., and Schneider, S. P., "Feedback Stabilized Laser Differential Interferometry for Supersonic Blunt Body Receptivity Experiments," *38th Aerospace Sciences Meeting & Exhibit*, American Institute of Aeronautics and Astronautics, 2000.

[5] Ceruzzi, A. P., and Cadou, C. P., "Turbulent Air Jet Investigation using Focused Laser Differential Interferometry," *53rd AIAA/SAE/ASEE Joint Propulsion Conference*, American Institute of Aeronautics and Astronautics, 2017.

[6] Harris, A. J., Kreth, P. A., Combs, C. S., and Schmisseur, J. D., "Laser Differential Interferometry and Schlieren as an Approach to Characterizing Freestream Disturbance Levels," American Institute of Aeronautics and Astronautics, 2018.

[7] Fulghum, M. R., "Turbulence Measurements in High-Speed Wind Tunnels Using Focusing Laser Differential Interferometry," Ph.D. thesis, The Pennsylvania State University, 12 2014.

[8] Schmidt, B. E., and Shepherd, J. E., "Analysis of focused laser differential interferometry," *Applied Optics*, Vol. 54, No. 28, 2015, pp. 8459–8472.

[9] Settles, G. S., and Fulghum, M. R., "The Focusing Laser Differential Interferometer, an Instrument for Localized Turbulence Measurements in Refractive Flows," *Journal of Fluids Engineering*, Vol. 138, No. 10, 2016, pp. 101402–101402–10.

[10] Lawson, J. M., Neet, M. C., Grossman, I. J., and Austin, J. M., "Characterization of a Focused Laser Differential Interferometer," American Institute of Aeronautics and Astronautics, 2019. doi:10.2514/6.2019-2296.

[11] Parziale, N. J., Shepher, J. E., and Hornung, H. G., "Differential Interferometric Measurement of Instability at Two Points in a Hypervelocity Boundary Layer," American Institute of Aeronautics and Astronautics, 2013.

[12] Parziale, N. J., Shepherd, J. E., and Hornung, H. G., "Free-stream density perturbations in a reflected-shock tunnel," *Experiments in Fluids*, Vol. 55, No. 2, 2014, p. 1665.

[13] Azzazy, M., Modarress, D., and Hall, R. M., "Optical Boundary-Layer Transition Detection in a Transonic Wind Tunnel," *AIAA Journal*, Vol. 27, No. 4, 1989, pp. 405–410. doi:10.2514/3.10127, URL https://doi.org/10.2514/3.10127.

[14] Parziale, N., "Slender-Body Hypervelocity Boundary-Layer Instability," Ph.D. thesis, California Institute of Technology, 05 2013.

[15] Jewell, J. S., Parziale, N. J., Leyva, I. A., and Shepherd, J. E., "Effects of Shock-Tube Cleanliness on Hypersonic Boundary Layer Transition at High Enthalpy," *AIAA Journal*, Vol. 55, No. 1, 2017, pp. 332–338. doi:10.2514/1.j054897.

[16] Houpt, A., and Leonov, S., "Focused Laser Differential Interferometer for Supersonic Boundary Layer Measurements on Flat Plate Geometries," American Institute of Aeronautics and Astronautics, 2018.

[17] Chou, A., Leidy, A. N., Bathel, B. F., King, R. A., and Herring, G. C., "Measurements of Freestream Fluctuations in the NASA Langley 20-Inch Mach 6 Tunnel," American Institute of Aeronautics and Astronautics, 2018.

[18] Weisberger, J. M., Bathel, B. F., Herring, G. C., King, R. A., Chou, A., and Jones, S. B., "Two-Point Focused Laser Differential Interferometry Second-Mode Measurements at Mach 6," *AIAA Aviation 2019 Forum*, 2019. doi:10.2514/6.2019-2903.

[19] Houpt, A., and Leonov, S., "Focused and Cylindrical-Focused Laser Differential Interferometer Characterization of SBR-50 at Mach 2," *AIAA Aviation 2019 Forum*, American Institute of Aeronautics and Astronautics, 2019. doi:10.2514/6.2019-3383, URL https://doi.org/10.2514/6.2019-3383.

[20] Ananthapadmanaban, R., McIntyre, T., Wheatley, V., and Mee, D. J., "Performance Analysis of FLDI Technique using Turbulent Jets," *IX Australian Conference on Laser Diagnostics*, 2020.

[21] Lawson, J. M., and Austin, J. M., "Expansion Tube Freestream Disturbance Measurements using a Focused Laser Differential Interferometer," *AIAA SciTech 2020 Forum*, American Institute of Aeronautics and Astronautics, 2020. doi:10.2514/6.2020-1064, URL https://doi.org/10.2514/6.2020-1064.

[22] Benitez, E. K., Jewell, J. S., and Schneider, S. P., "Focused Laser Differential Interferometry for Hypersonic Flow Instability Measurements with Contoured Tunnel Windows," *AIAA SciTech 2020 Forum*, American Institute of Aeronautics and Astronautics, 2020. doi:10.2514/6.2020-1282, URL https://doi.org/10.2514/6.2020-1282.

[23] Jewell, J. S., Parziale, N. J., Lam, K.-Y., Hagen, B. J., and Kimmel, R. L., "Disturbance and Phase Speed Measurements for Shock Tubes and Hypersonic Boundary-Layer Instability," *32nd AIAA Aerodynamic Measurement Technology and Ground Testing Conference*, American Institute of Aeronautics and Astronautics, 2016.

[24] Ceruzzi, A., and Cadou, C. P., "Simultaneous Velocity and Density Gradient Measurements using Two-Point Focused Laser Differential Interferometry," American Institute of Aeronautics and Astronautics, 2019. doi:10.2514/6.2019-2295.

[25] Ceruzzi, A. P., Callis, B. O., Weber, D. C., and Cadou, C. P., "Application of Focused Laser Differential Interferometry (FLDI) in a Supersonic Boundary Layer," *AIAA SciTech 2020 Forum*, American Institute of Aeronautics and Astronautics, 2020. doi:10.2514/6.2020-1973, URL https://doi.org/10.2514/6.2020-1973.

[26] Bathel, B. F., Weisberger, J. M., Herring, G. C., King, R. A., Jones, S. B., Kennedy, R. E., and Laurence, S. J., "Two-point, parallel-beam focused laser differential interferometry with a Nomarski prism," *Applied Optics*, Vol. 59, No. 2, 2020. doi:10.1364/AO.59.000244.

[27] Wadhams, T. P., MacLean, M., and Parker, R., "Sharp Cone Boundary Layer Transition and Stability at Mach 10," *22nd AIAA International Space Planes and Hypersonics Systems and Technologies Conference*, American Institute of Aeronautics and Astronautics, 2018. doi:10.2514/6.2018-5323, URL https://doi.org/10.2514/6.2018-5323.

[28] Hameed, A., Parziale, N. J., Paquin, L. A., Butler, C., and Laurence, S. J., "Hypersonic Slender-Cone Boundary-Layer Instability in the UMD HyperTERP Shock Tunnel," *AIAA SciTech 2020 Forum*, American Institute of Aeronautics and Astronautics, 2020. doi:10.2514/6.2020-0362, URL https://doi.org/10.2514/6.2020-0362.